ELSEVIER

Hearing Research 171 (2002) 13–31

HEARING RESEARCH

www.elsevier.com/locate/heares

Tuning and timing of excitation and inhibition in primary auditory nerve fibers

Edwin R. Lewis [a,*], Kenneth R. Henry [b], Walter M. Yamada [c]

[a] *Department of Electrical Engineering and Computer Science, University of California, Berkeley, CA 94720, USA*
[b] *Department of Psychology, University of California, Davis, CA 95616, USA*
[c] *Biomedical Simulations Resource, University of Southern California, Los Angeles, CA 90089, USA*

Received 21 August 2001; accepted 4 December 2001

Abstract

Information about the tuning and timing of excitation, adaptation and suppression in an auditory primary afferent axon can be obtained from the second-order Wiener kernel. Through the process of singular-value decomposition, this information can be extracted from the kernel and displayed graphically in separate two-dimensional images for excitation and inhibition[1]. For low- to mid-frequency units, the images typically include checkerboard patterns. For all units they may include patterns of parallel diagonal lines. The former represent non-linearities in the phase-locked (ac) response of the unit; the latter reflect non-linear envelope-following (dc) responses. Examples of detailed interpretation are presented for three amphibian-papillar units from the American bullfrog. The second-order Wiener kernel itself is derived from second-order reverse correlation between spikes and a continuous, non-repeating, broad-band white-noise stimulus.

Key words: Tuning; Temporal response; Adaptation; Suppression; Reverse correlation; Frog amphibian papilla

1. Introduction

For a primary auditory afferent unit, the second-order Wiener kernel provides a two-dimensional visual image of the unit's second-order non-linear dynamics (Eggermont, 1993; van Dijk et al., 1994, 1997a,b; Yamada et al., 1996; Yamada, 1997; Yamada and Lewis, 1999). For a low-frequency auditory unit, the most dominant feature of this image typically is a checkerboard pattern of light and dark squares (van Dijk et al., 1997a; Yamada et al., 1996). For a high-frequency unit, the most dominant feature typically is a pattern of parallel diagonal lines (van Dijk et al., 1997a; Yamada, 1997). Simple array arithmetic allows us to decompose the second-order kernel into two separate images, one corresponding solely to positive changes in spike rate (e.g. excitatory processes), the other corresponding solely to negative changes in spike rate (e.g. inhibitory processes). It also allows us to attach physiological meaning to features such as the checkerboard and parallel diagonal line patterns. In this paper we apply this approach to data from the American bullfrog (*Rana catesbeiana*). In a subsequent paper, we apply it to the Mongolian gerbil (*Meriones unguiculatus*).

The first-order Wiener kernel (commonly known in the hearing research community as the REVCOR function) is simply a waveform segment that can be interpreted as a truncated estimate of the linear component of the unit's impulse response. The kernel is produced by reverse correlation of a white-noise stimulus and the spikes produced by that stimulus in the auditory unit's axon (de Boer and Kuyper, 1968; de Boer and de Jongh, 1978). In practice, it is computed from noise-stimulus waveforms that are digitized with a fixed sam-

* Corresponding author. Tel.: +1 (510) 642 6954; Fax: +1 (510) 643 8426.
E-mail address: lewis@eecs.berkeley.edu (E.R. Lewis).

[1] In this paper, we use the term *inhibition* to include all of those phenomena (such as adaptation and rate suppression) that result in reduction of instantaneous spike rate in a primary auditory afferent axon; it does not imply involvement of inhibitory synapses. We use *excitation* to include all of those phenomena that result in increase of instantaneous spike rate.

0378-5955/02/$ – see front matter
PII: S0378-5955(02)00290-3

pling rate; the reciprocal of the sampling rate defines the unit of temporal resolution, or *instant*, in the resulting discrete-time representation. Current practice usually employs the following steps: (1) digitize both the white-noise stimulus and the neural recording at a rate of m samples per second (making each instant equal to $(1/m)$th of a second); (2) estimate the instant (sampling interval) during which the peak of each spike occurred; (3) select the segment of white-noise stimulus (the n successive samples of stimulus sound pressure) that occurred at that instant and at the $n-1$ instants immediately preceding it, e.g. for $n=4$

$$S_i = i\text{th stimulus segment} = a_i\ b_i\ c_i\ d_i \tag{1}$$

(4) reverse the segment in time,

$$S_i(\text{rev}) = d_i\ c_i\ b_i\ a_i \tag{2}$$

(5) compute the average of all such n-sample segments; and (6) multiply the result by an appropriate scale factor K (normalizing for mean spike rate and noise-stimulus power level) (Schetzen, 1980; van Dijk et al., 1994); the unit of the normalized kernel typically would be 1.0 spike/s per Pa; e.g. for N spikes

$$h_1(\tau) = K[\tilde{d}\ \tilde{c}\ \tilde{b}\ \tilde{a}] = h_1(0)\ h_1(1)\ h_1(2)\ h_1(3) \tag{3}$$

where

$$\tilde{a} = \frac{1}{N}\sum_{i=1}^{N} a_i$$

Thus, in practice, each white-noise segment is stored as a linear array of n sound-pressure values; and the first-order kernel, h_1, is a linear array of n normalized average sound-pressure values. Thus, $h_1(0)$ is the normalized average value of the noise sound pressure at the instant of the spike peak; $h_1(1)$ is the normalized average value of the noise sound pressure in the instant immediately preceding the spike peak, and so forth.

The second-order kernel is computed by repeating the first four steps used for the first-order kernel, then proceeding through the following steps (Marmarelis and Marmarelis, 1978; van Dijk et al., 1994): (5) take the outer product of each reversed segment (S_i(rev)) with itself (see Table 1)

$$\begin{bmatrix} a_id_i & a_ic_i & a_ib_i & a_i^2 \\ b_id_i & b_ic_i & b_i^2 & b_ia_i \\ c_id_i & c_i^2 & c_ib_i & c_ia_i \\ d_i^2 & d_ic_i & d_ib_i & d_ia_i \end{bmatrix} \tag{4}$$

(6) compute the average over all such $n\times n$ arrays,

$$\begin{bmatrix} \tilde{ad} & \tilde{ac} & \tilde{ab} & \tilde{aa} \\ \tilde{bd} & \tilde{bc} & \tilde{bb} & \tilde{ba} \\ \tilde{cd} & \tilde{cc} & \tilde{cb} & \tilde{ca} \\ \tilde{dd} & \tilde{dc} & \tilde{db} & \tilde{da} \end{bmatrix} \tag{5}$$

where, for example, for N spikes

$$\tilde{ad} = \frac{1}{N}\sum_{i=1}^{N} a_id_i \tag{6}$$

(7) subtract the covariance matrix (cov) of the noise stimulus (a symmetric $n\times n$ array of values computed in exactly the same way, but from all possible n-sample segments of the white-noise stimulus). Then (8) multiply the result by an appropriate scale factor K_2 (normalizing for mean spike rate and noise-stimulus power level) (Schetzen, 1980; van Dijk et al., 1994).

$$cov = \begin{bmatrix} \tilde{AD} & \tilde{AC} & \tilde{AB} & \tilde{AA} \\ \tilde{BD} & \tilde{BC} & \tilde{BB} & \tilde{BA} \\ \tilde{CD} & \tilde{CC} & \tilde{CB} & \tilde{CA} \\ \tilde{DD} & \tilde{DC} & \tilde{DB} & \tilde{DA} \end{bmatrix} \tag{7}$$

$$h_2(\tau_1,\tau_2) = K_2 \begin{bmatrix} \tilde{ad}-\tilde{AD} & \tilde{ac}-\tilde{AC} & \tilde{ab}-\tilde{AB} & \tilde{aa}-\tilde{AA} \\ \tilde{bd}-\tilde{BD} & \tilde{bc}-\tilde{BC} & \tilde{bb}-\tilde{BB} & \tilde{ba}-\tilde{BA} \\ \tilde{cd}-\tilde{CD} & \tilde{cc}-\tilde{CC} & \tilde{cb}-\tilde{CB} & \tilde{ca}-\tilde{CA} \\ \tilde{dd}-\tilde{DD} & \tilde{dc}-\tilde{DC} & \tilde{db}-\tilde{DB} & \tilde{da}-\tilde{DA} \end{bmatrix}$$

$$= \begin{bmatrix} h_2(3,0) & h_2(3,1) & h_2(3,2) & h_2(3,3) \\ h_2(2,0) & h_2(2,1) & h_2(2,2) & h_2(2,3) \\ h_2(1,0) & h_2(1,1) & h_2(1,2) & h_2(1,3) \\ h_2(0,0) & h_2(0,1) & h_2(0,2) & h_2(0,3) \end{bmatrix} \tag{8}$$

Thus, $h_2(0,0)$ is the normalized average of the square of the noise-stimulus amplitude that occurred at the instant of the spike peak, less the normalized average square of the noise-stimulus amplitude; $h_2(1,1)$ is the normalized average of the square of the noise-stimulus amplitude that occurred one instant before the spike peak, less the normalized average square of the noise-stimulus amplitude; and $h_2(k,j)$ is the normalized average of the product of the noise-stimulus amplitudes that occurred k and j instants before the spike peak, less the normalized average product of noise-stimulus amplitudes $k-j$ instants apart.

Table 1
Outer product of the vector $d_i\ c_i\ b_i\ a_i$ with itself

a_i	a_id_i	a_ic_i	a_ib_i	a_ia_i
b_i	b_id_i	b_ic_i	b_ib_i	b_ia_i
c_i	c_id_i	c_ic_i	c_ib_i	c_ia_i
d_i	d_id_i	d_ic_i	d_ib_i	d_ia_i
	d_i	c_i	b_i	a_i

By virtue of the manner in which it is constructed, the second-order Wiener kernel (h_2) for an auditory unit is a square ($n\times n$) array of real numbers, whose values are symmetrically arranged about the rising diagonal of the square – as they are in the following (4×4) array:

$$\begin{bmatrix} \alpha & \beta & \gamma & \delta_4 \\ \varepsilon\xi & \delta_3 & \gamma & \\ \eta & \delta_2 & \xi & \beta \\ \delta_1 & \eta & \varepsilon & \alpha \end{bmatrix} \tag{9}$$

where each letter represents a positive or negative real number, and the rising diagonal comprises the numbers δ_i. For such an array of numbers, the matrix operation known as *singular-value decomposition* yields an especially simple result (Yamada, 1997), allowing us to reconstruct h_2 from a weighted set of n waveforms (known as *singular vectors*).

$$h_2(\tau_1,\tau_2)=\sum_{j=1}^{n}k_j\hat{h}_j(\tau_1)\hat{h}_j(\tau_2) \tag{10}$$

For each singular vector, $\hat{h}_j$, in this formulation, the corresponding weight, k_j, can be either a positive or a negative real number (see Appendix).

Having computed the kernels, one can insert them into the Wiener series (see Marmarelis and Marmarelis, 1978; Rugh, 1981; Schetzen, 1980) to obtain predictions of the response, $r(t)$, of the auditory unit to a new stimulus waveform, $p(t)$, of arbitrary complexity.

$$\begin{aligned} r(t) &= h_0+\sum_{\tau=0}^{n-1}h_1(\tau)p(t-\tau)+ \\ &\sum_{\tau_2=0}^{n-1}\sum_{\tau_1=0}^{n-1}h_2(\tau_1,\tau_2)p(t-\tau_1)p(t-\tau_2)+\ldots \\ &= r_0+r_1(t)+r_2(t)+\ldots \end{aligned} \tag{11}$$

where h_0 was the mean spike rate in the presence of the white noise; t is time (number of instants) from the beginning of the stimulus waveform; $r(t)$ is instantaneous spike rate; and $p(t)$ is sound pressure. Thus, if the stimulus waveform, $p(t)$, were repeated M times, $r(t)$ would predict the content of the tth bin of the peristimulus time histogram (PSTH) divided by the total time represented by each bin, M/m (m being the rate at which the noise was sampled). Singular-value decomposition of h_2 allows us to simplify the second-order term, $r_2(t)$, in a revealing manner. Inserting the right-hand side of Eq. 10 into the third term of Eq. 11, we have

$$\begin{aligned} r_2(t) &= \sum_{\tau_1=0}^{n-1}\sum_{\tau_2=0}^{n-1}\left[\sum_{j=1}^{n}k_j\hat{h}_j(\tau_1)\hat{h}_j(\tau_2)\right]p(t-\tau_1)p(t-\tau_2) \\ &= \sum_{j=1}^{n}k_j\sum_{\tau_1=0}^{n-1}\hat{h}_j(\tau_1)p(t-\tau_1)\sum_{\tau_2=0}^{n-1}\hat{h}_j(\tau_2)p(t-\tau_2) \\ &= \sum_{j=1}^{n}k_j\left[\sum_{\tau=0}^{n-1}\hat{h}_j(\tau)p(t-\tau)\right]^2=\sum_{j=1}^{n}\hat{r}_j(t) \end{aligned} \tag{12}$$

where

$$\hat{r}_j(t)=k_j\left[\sum_{\tau=0}^{n-1}\hat{h}_j(\tau)p(t-\tau)\right]^2$$

The form (first-order convolution) of the first-order term of the Wiener series represents a linear filtering process. The response $r_1(t)$ would be the output of the filter when $p(t)$ was its input; the impulse response of the filter would be $h_1(t)$. Similarly, the response $\hat{r}_j(t)$ in Eq. 12 would be the square of the output of a linear filter when $p(t)$ was its input; the impulse response of this filter would be $\hat{h}_j(t)$. Thus $r_2(t)$ can be interpreted to be a weighted sum of the squares of the outputs of n linear filters, each with its own impulse response or *filter function*.

Notice that, regardless of the form of $p(t)$, $\hat{r}_j(t)$ is either entirely positive or entirely negative, depending on the sign of k_j. This allows one to decompose the second-order kernel into two $n\times n$ arrays, the excitatory component ($h_{2\mathrm{exc}}$) reconstructed from all singular vectors with positive weights, and the inhibitory component ($h_{2\mathrm{inh}}$) reconstructed from all singular vectors with negative weights.

$$h_2(\tau_1,\tau_2)=h_{2\mathrm{exc}}(\tau_1,\tau_2)+h_{2\mathrm{inh}}(\tau_1,\tau_2) \tag{13}$$

where

$$\begin{aligned} h_{2\mathrm{exc}}(\tau_1,\tau_2) &= \sum_{j=1}^{n}k_j\hat{h}_j(\tau_1)\hat{h}_j(\tau_2) \qquad \text{for } k_j>0 \\ h_{2\mathrm{inh}}(\tau_1,\tau_2) &= \sum_{j=1}^{n}k_j\hat{h}_j(\tau_1)\hat{h}_j(\tau_2) \qquad \text{for } k_j<0 \end{aligned} \tag{14}$$

2. Checkerboard patterns

The excitatory component of the second-order Wiener kernel for each low-frequency frog or gerbil axon (N of several hundreds) exhibited a robust checkerboard pattern. This pattern invariably arose from the outer product of one, dominant, singular vector with

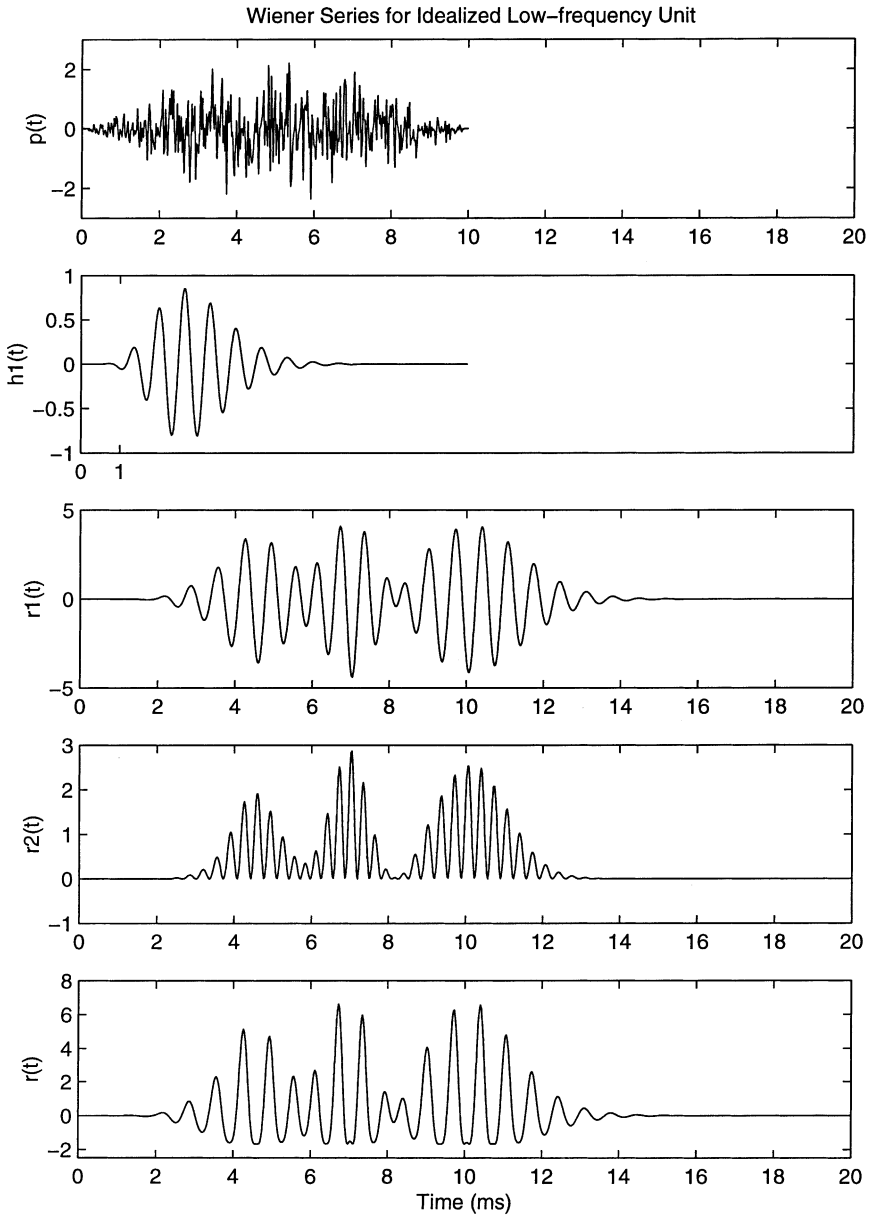

Fig. 1. Predictions from a simple model of a 1.5-kHz cochlear unit, with $h_0 = 0$ and h_2 equal to 0.15 times the outer product of h_1 with itself. First panel (top): The input is a complex waveform, $p(t)$. Second panel: We have constructed h_1 as a truncated gammatone function. Third panel: The convolution of $p(t)$ with $h_1(t)$ yields the first-order term, $r_1(t)$, of the Wiener series. Fourth panel: With this simple model, the second-order term, $r_2(t)$, of the Wiener series is $0.15[r_1(t)]^2$. Fifth panel (bottom): The modeled PSTH, $r(t)$, predicted by the Wiener series approximates a phase-locked response, clipped at zero spikes per second. Prediction of abrupt clipping at zero spikes per second would require inclusion of higher-order terms in the Wiener series.

itself (typically the highest-ranking singular vector) (see Table 1); and that singular vector invariably had an oscillatory shape that matched almost precisely the shape of the first-order kernel (REVCOR function). In other words, in each case, the shape (but not the amplitude) of the checkerboard pattern in $h_{2\mathrm{exc}}$ could be reconstructed as the outer product of h_1 with itself. This makes the interpretation of the checkerboard pattern in $h_{2\mathrm{exc}}$ very simple. The predicted response of the unit to a complex waveform will include a linearly-filtered version of that waveform (the first-order term of the Wiener series of Eq. 11) plus the square of the same linearly-filtered version, weighted by a positive number. This represents a waveform that is filtered and subsequently distorted in such a way that its positive excursions are enlarged and its negative excursions reduced. The effect is modeled in Fig. 1. Here the first- and second-order terms of a Wiener series are combined to yield a prediction of the PSTH (bottom panel) in response to a complex waveform (top panel).

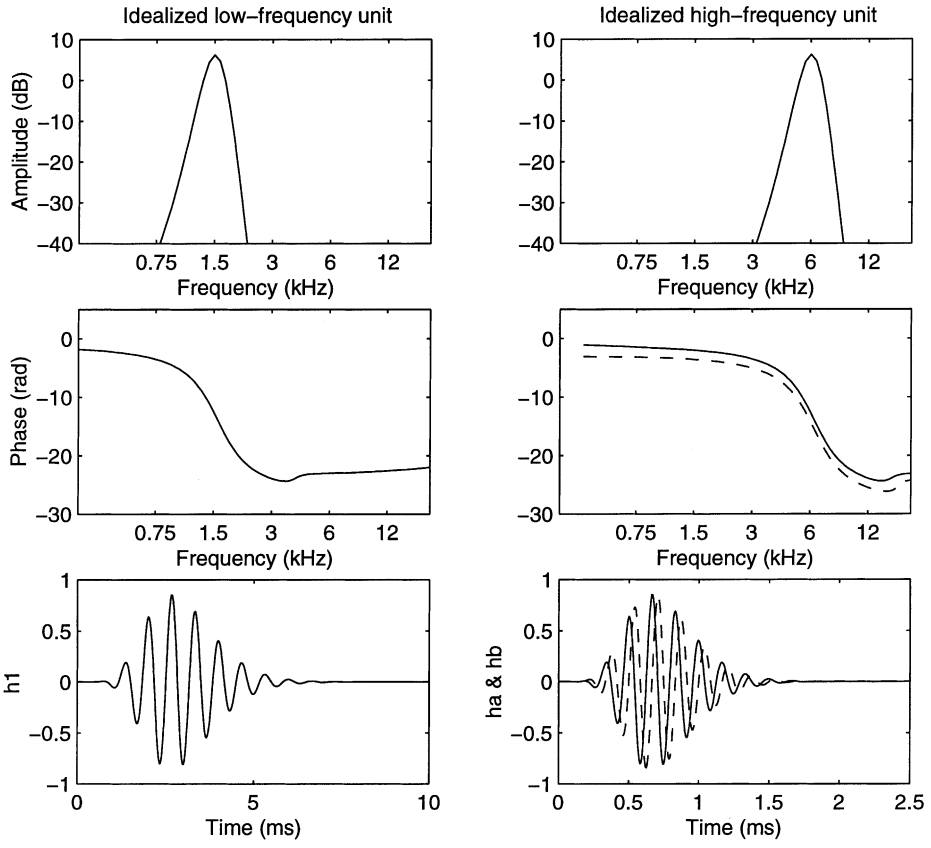

Fig. 2. Model filter functions. Left-hand panels: for a low-frequency unit, an eighth-order gammatone function and the amplitude and phase components of its discrete Fourier transform (DFT). Right-hand panels: for a high-frequency unit a quadrature pair of eighth-order gammatone functions and their DFTs.

By itself, the first-order term, $r_1(t)$, of the Wiener series predicts both positive and negative swings in the instantaneous spike rate. The negative swings, of course, can be seen only if they are superimposed on background activity (represented by h_0). When the background activity is inadequate, the negative excursions will be clipped at zero spikes per second. In that case, the second-order term provides an approximation to the clipping. For cases in which the background rate (h_0) is sufficient to prevent clipping, the second-order term simply represents accentuation of the positive-going excursions relative to the negative-going excursions of the phase-locked response. This commonly-seen form of even-order distortion can be explained in terms of a negative slope in the probability density function of the unit's internal noise amplitude in the vicinity of threshold at the spike trigger (see Lewis and Henry, 1995).

The 1.5-kHz gammatone function used in the model of Fig. 1 is presented again in the bottom left-hand panel of Fig. 2. The phase and amplitude components of its discrete Fourier transform (DFT) are shown directly above it. The upper panel of Fig. 3 shows h_2, with its bold checkerboard pattern, constructed as the outer product of this h_1 with itself (weighting factor = +1.0). For the model of Fig. 1, this second-order kernel was scaled (arbitrarily) by the factor +0.15.

3. Patterns comprising parallel diagonal lines

Under singular-value decomposition, a clear pattern of parallel diagonal lines in the second-order Wiener kernel of a frog or gerbil axon ($N > 100$) invariably has yielded a pair of oscillatory singular vectors with essentially identical shapes, but 90° out of phase (i.e. *in quadrature*) with one another. When the weights of these two singular vectors are nearly equal, the corresponding pattern consists of parallel diagonal lines; when they are unequal, a checkerboard pattern is superimposed on the pattern of parallel lines. In Fig. 2 (right-hand panels) and Fig. 3 (bottom panel) we have modeled the situation with equal weights for a 6-kHz cochlear unit. The quadrature pair of singular vectors (bottom right-hand panel of Fig. 2) comprises a gamma sine function and a gamma cosine function. The phase and amplitude components of their DFTs are shown directly above them. The lower panel of Fig. 3 shows

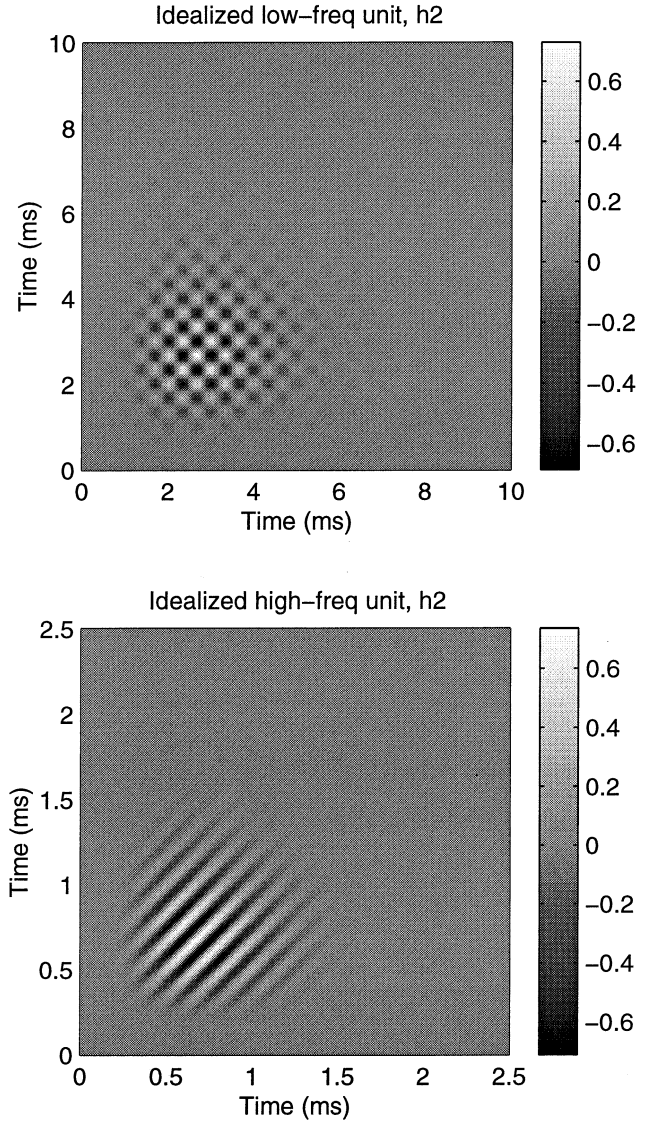

Fig. 3. Second-order Wiener kernels derived from the filter functions in Fig. 2.

h_2 constructed as the sum of the outer products of each of these singular vectors with itself.

Patterns of parallel diagonal lines, without obvious checkerboard patterns superimposed on them, were typical of h_{2exc} for units whose characteristic frequencies (CFs) were above the frequencies at which phase locking occurs. For units with somewhat lower CFs, with checkerboard superimposed on parallel diagonal lines, the shapes of the higher-ranking members of the quadrature pairs of singular vectors invariably were close matches to those of the first-order kernels, $h_1(t)$. Thus, the checkerboard component of h_{2exc} would be interpreted in the same way that it is for low-CF units: the predicted PSTH would include a linearly-filtered version of the input waveform, plus the square of that same linearly-filtered version, weighted appropriately.

When the weights of the members of a quadrature pair of singular vectors are equal, interpretation of their contribution to the predicted response is relatively simple (see Yamada and Lewis, 1999). Eq. 12 tells us that the contribution comprises the sum of the squares of the outputs of two linear filters – the impulse responses of which are the two singular vectors. Before they are squared these two output waveforms themselves are in quadrature. The sum of the square of two waveforms in quadrature is the square of the positive half envelope of either filtered waveform. This is modeled in Fig. 4. A complex input waveform, $p(t)$, is convolved with each of the two members, h_a and h_b, of the quadrature pair (same pair as bottom right panel of Fig. 2). This yields the (filtered) waveforms y_a and y_b. These are squared and summed to yield the predicted PSTH in the bottom panel of Fig. 4. If, instead of a burst of band-limited noise, the stimulus $p(t)$ in Fig. 4 had been a continuing sinusoid (i.e. a tonal stimulus), $r_2(t)$ would have been a positive constant (e.g. a positive dc contribution to spike rate). Thus, the class of responses represented by patterns of parallel diagonal lines in h_{2exc} includes those often labeled *excitatory dc responses*.

4. Examples from the frog amphibian papilla

American bullfrogs (*R. catesbeiana*) were anesthetized by a combination of sodium pentobarbital and ketamine. The auditory nerve was exposed by a ventral approach, through the roof of the mouth. Recordings were made from single afferent axons, penetrated with glass micropipette electrodes. Auditory stimuli were applied through a closed-field system that included a probe microphone for sensing the sound-pressure level at the tympanum. Single-unit spikes and tympanic sound-pressure level were recorded together on separate channels of a cassette tape recorder, to be analyzed later off-line. Specific details, including dosages and equipment, have been published previously (Yamada and Lewis, 1999)[2].

The examples shown here were selected for illustrative purposes. The upper panel in Fig. 5 is a second-order Wiener kernel ($n = 200$) taken over 3900 spikes from a 300-Hz amphibian-papillar unit (in response to white noise, 90 dB SPL, 100 Hz to 3.8 kHz). Singular-value decomposition of h_2 produced 200 singular vectors; the weights of the highest ranking of these are shown in Fig. 6. All 200 singular vectors were used in the construction of the excitatory and inhibitory components of h_2 (middle and bottom panels, respectively, of Fig. 5). Fig. 7 (bottom panel, dashed line) shows the

[2] All animal experiments were performed in accordance with protocols approved by the UC Berkeley Animal Care and Use Committee (protocol # R081-1097).

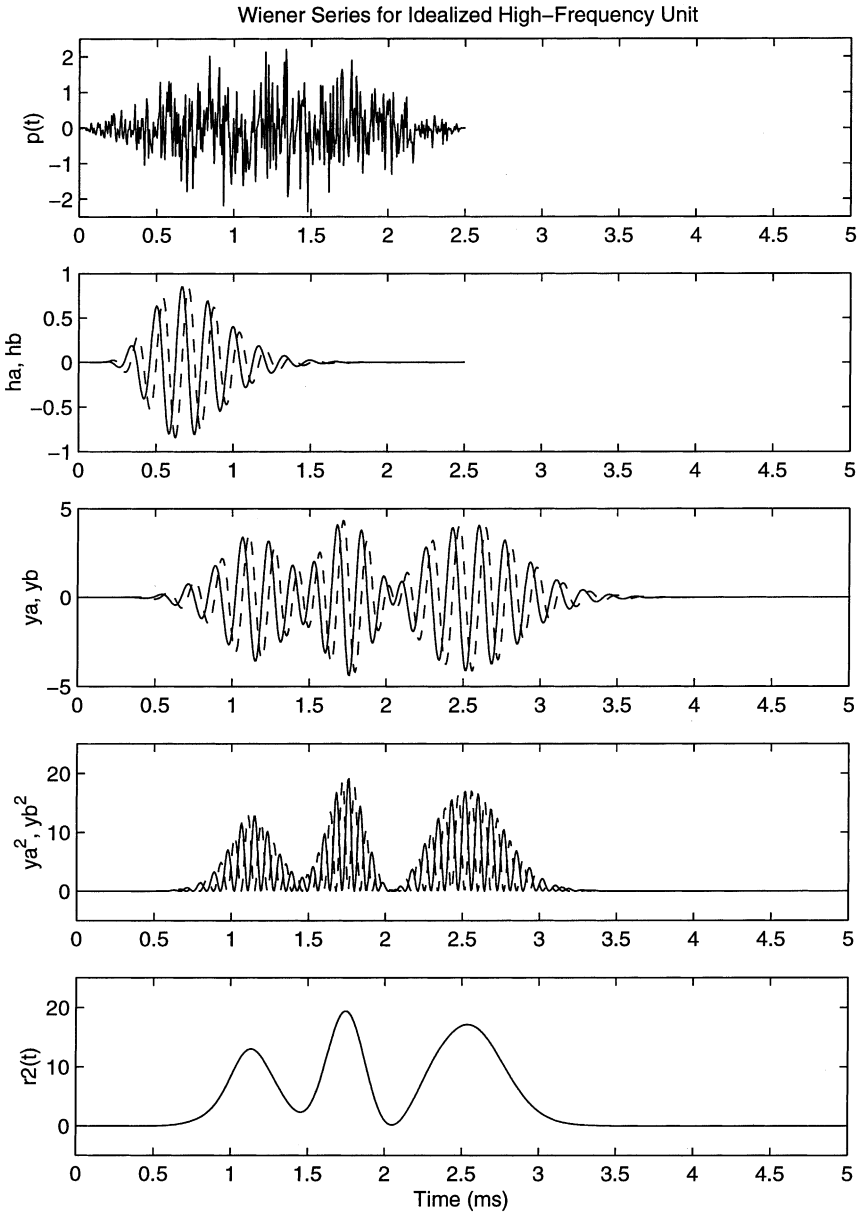

Fig. 4. Predictions from a model of a 6-kHz cochlear unit, with $h_0 = 0$, $h_1 = 0$, and h_2 being the equally-weighted sum of the outer products of each member of the quadrature pair h_a and h_b with itself. First panel (top): The input is the complex waveform, $p(t)$ (note time-scale change from Fig. 1). Second panel: We have constructed h_a and h_b as quadrature gammatone functions. Third panel: The convolution of $p(t)$ with h_a and h_b yields the filtered functions, y_a and y_b, respectively. Fourth panel: Each of the functions y_a and y_b is squared. Fifth panel (bottom): The modeled PSTH, $r(t) = y_a^2 + y_b^2$, predicted by the Wiener series is the square of the positive half envelope of y_a and y_b.

highest-ranking singular vector (SV_1, corresponding to rank 1 in Fig. 6) plotted together with the first-order Wiener kernel, h_1 (solid line), for this unit. The amplitude and phase components of the DFTs of these functions are plotted above them. As discussed previously in Section 2, the fact that the shapes of h_1 and SV_1 are so nearly identical allows us to interpret them both as reflecting a single linear filter, with some square-law distortion (e.g. clipping) at its output. Fig. 8 (bottom panel, dashed line) shows the second-ranked singular vector, SV_2, plotted together with SV_1 (solid line). Clearly SV_1 (in part) and SV_2 compose a quadrature pair, which must reflect underlying parallel diagonal lines in h_2 and in its excitatory component, h_{2exc}. In Fig. 6 one can see that the weight for SV_1 is approximately 40, and that for SV_2 is approximately 9. Thus the fraction of SV_1 that contributes to the diagonal parallel lines is approximately 9/40, and the fraction that contributes to the checkerboard pattern is approximately 31/40. This in turn implies that 31/40 of SV_1 contributes to square-law distortion of the response that is phase-locked to the linearly-filtered version of

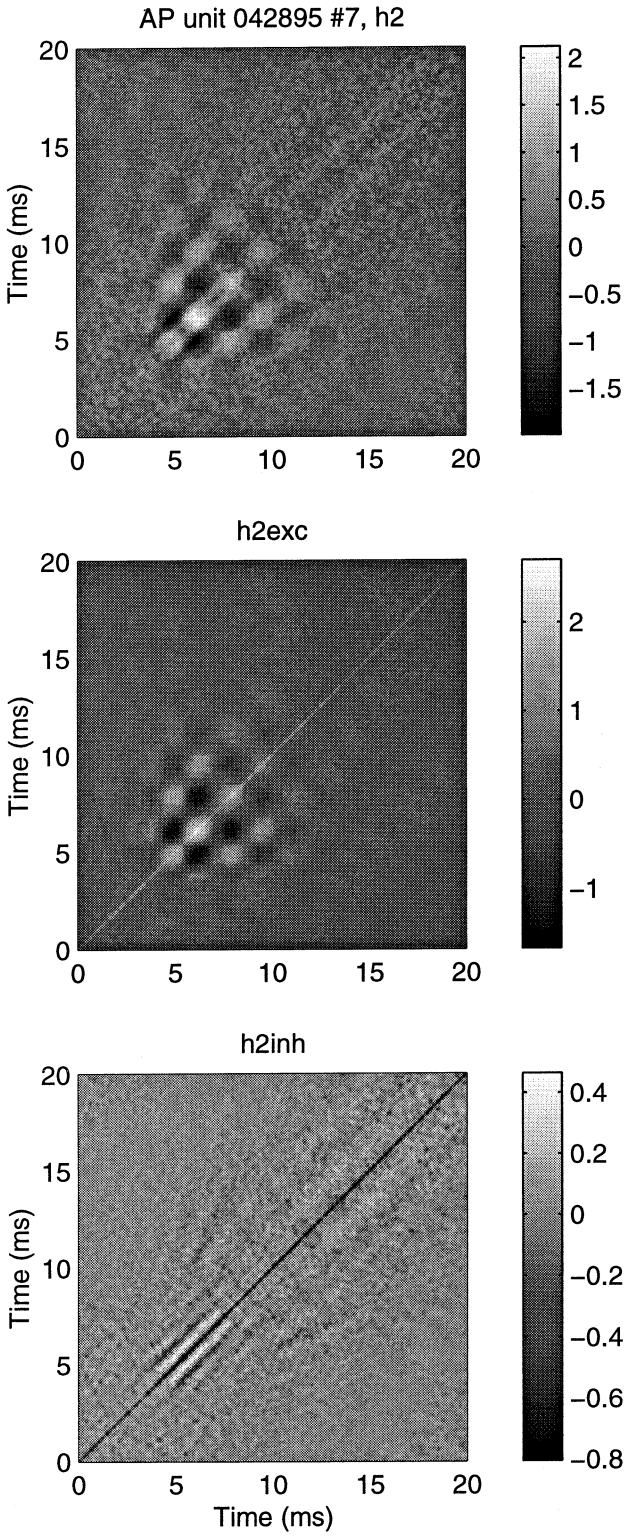

Fig. 5. Second-order Wiener kernel, along with its excitatory and inhibitory components, from a bullfrog amphibian-papillar unit.

the stimulus waveform; 9/40 of SV_1 contributes to the response that is phase-locked to the square of the envelope of that filtered waveform.

Fig. 6 shows that the weights of the third, fourth and fifth ranked singular vectors (SV_3, SV_4 and SV_5) are negative. This means that they contribute to h_{2inh} rather than h_{2exc}. In addition to the dark line along its main (rising) diagonal, the most obvious features of h_{2inh} in Fig. 5 are a pattern of diagonal parallel lines in the vicinity of 5 ms and another (more faint and possibly overlaid with checkerboard) between 10 and 20 ms. Whereas h_{2exc} represents strictly additive (positive) contributions to the instantaneous spike rate ($r_2(t)$ in Eq. 12), h_{2inh} represents strictly subtractive (negative) contributions. Thus, while a pattern of parallel diagonal lines in h_{2exc} represents an added component of instantaneous spike rate that follows the square of the envelope of a filtered waveform (including positive dc response to a constant-amplitude tone), that sort of pattern in h_{2inh} represents the subtraction of such a component (including a negative dc response to a constant-amplitude tone).

One can see that the periodicity of the pattern in the vicinity of 5 ms in h_{2inh} reflects tuning to a frequency that is higher than that represented by the checkerboard pattern in h_{2exc}. The periodicity of the pattern between 10 and 20 ms in h_{2inh} is very similar to that of the checkerboard pattern in h_{2exc}, evidently reflecting tuning to approximately the same frequency. This conclusion is supported by the tuning of the DFTs of SV_3 and SV_4 (Fig. 9, top panel). These two singular vectors clearly represent both patterns, the higher-frequency pattern around 5 ms and the lower-frequency pattern between 10 and 20 ms (compare the bottom panels of Figs. 5 and 9). Their DFTs show tuning peaks at approxi-

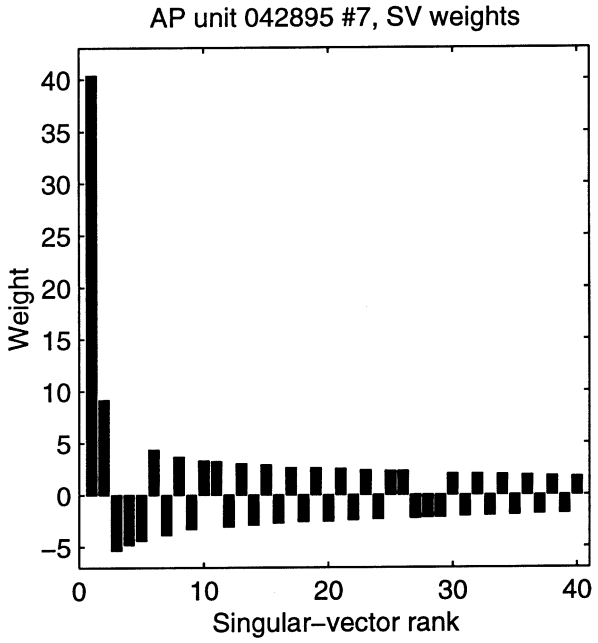

Fig. 6. Weights for the 40 highest-ranking singular vectors of the Wiener kernel of Fig. 5.

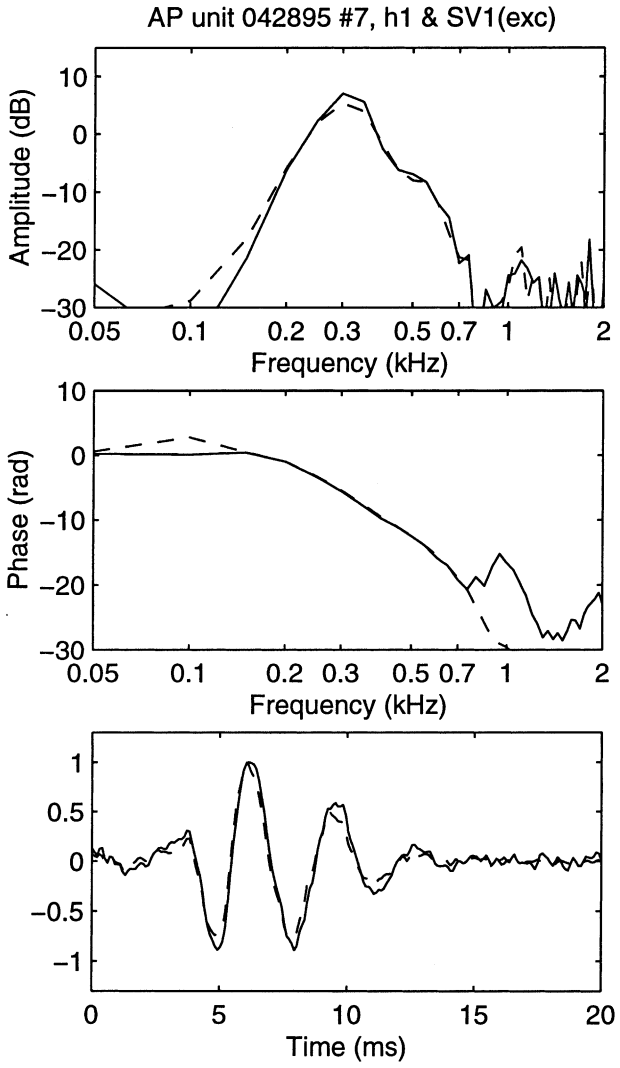

Fig. 7. First-order Wiener kernel (bottom panel, solid line) and the highest-ranking singular vector (bottom panel, dashed line) of the second-order Wiener kernel of the amphibian-papillar unit of Fig. 5. For comparison of shapes, both waveforms were normalized to yield a peak positive value of 1.0. The corresponding DFTs are shown in the top and middle panels.

mately 850 Hz and 300 Hz, respectively for the two patterns.

We now can incorporate the information contained in Figs. 5–9 into a single interpretation in terms of both time and frequency. If we take the origin of the time plots in these figures (all three panels of Fig. 5, bottom panels of Figs. 7–9) to represent the present moment in time, then we have the following components in the present instantaneous spike rate, $r(t)$: (1) From h_1, there is a component of the present instantaneous spike rate that is phase-locked to a filtered version of the stimulus constituents that occurred approximately 4–10 ms ago and had spectral energy in the vicinity of 300 Hz (Fig. 7). (2) From $h_{2\mathrm{exc}}$, there is additive square-law distortion of component 1 and a small additive contribution proportional to the square of the envelope of component 1. (3) From $h_{2\mathrm{inh}}$, there is a subtractive component of the present instantaneous spike rate proportional to the square of the envelope of a filtered version of the stimulus constituents that occurred approximately 4–7 ms ago and had spectral energy in the vicinity of 850 Hz. (4) Also from $h_{2\mathrm{inh}}$, there is a subtractive component proportional to the square of the envelope of a filtered version of the stimulus constituent that occurred approximately 10–20 ms ago and had spectral energy in the vicinity of 300 Hz.

Thus, the response to a brief 300-Hz stimulus would be reduced by the presence of an earlier 300-Hz stimulus. We presume that this corresponds to the phenomenon commonly labelled *adaptation*. The response to the brief 300-Hz stimulus also would be reduced by the simultaneous presence of an 850-Hz stimulus. We presume that this corresponds to the phenomenon com-

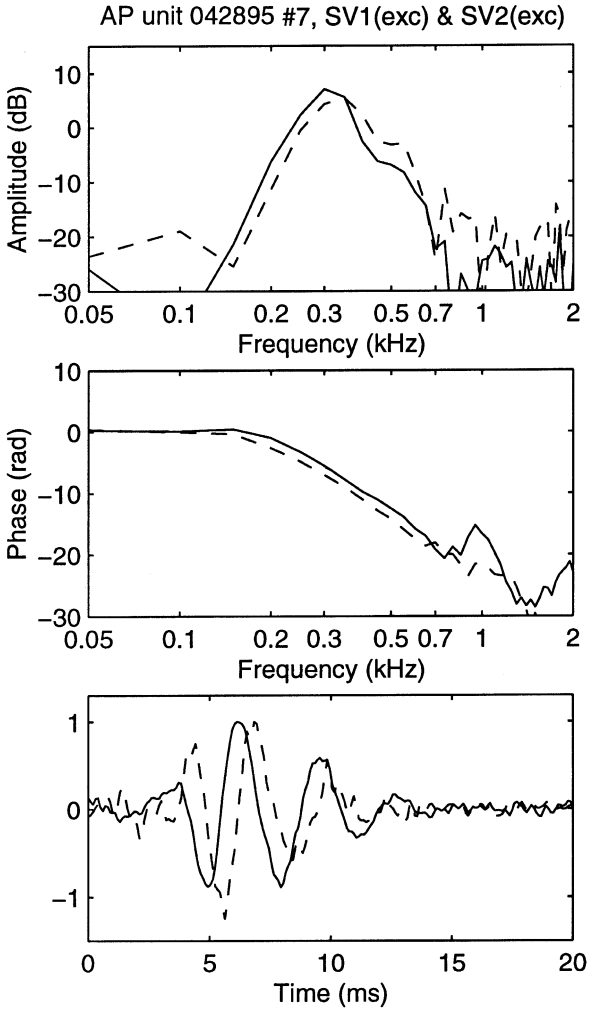

Fig. 8. Highest-ranking pair of singular vectors of the second-order Wiener kernel of Fig. 5, normalized as in Fig. 7, along with their DFTs. These two vectors form an excitatory quadrature pair, embodying excitatory timing and tuning.

monly labelled *suppression*. The bottom panel of Fig. 5 shows what appears to be a graded transition between these two phenomena (between approximately 8 and 12 ms). We often find this feature in the h_{2inh} from a frog amphibian-papillar unit or a gerbil cochlear unit. It is clear that in h_2 and its singular vectors, we have evidence concerning not only the tuning of these two phenomena, but also their timing.

The second-order Wiener kernel described in Figs. 10–14 was taken over 4100 spikes from a 560-Hz amphibian-papillar unit (in response to white noise, 82 dB SPL, 100 Hz to 3.8 kHz). In frog amphibian-papillar units, phase locking becomes weak at frequencies above approximately 500 Hz (Hillery and Narins, 1987). For this 560-Hz unit, the weights for SV_1 and SV_2 are nearly equal; h_{2exc} therefore reflects largely an additive

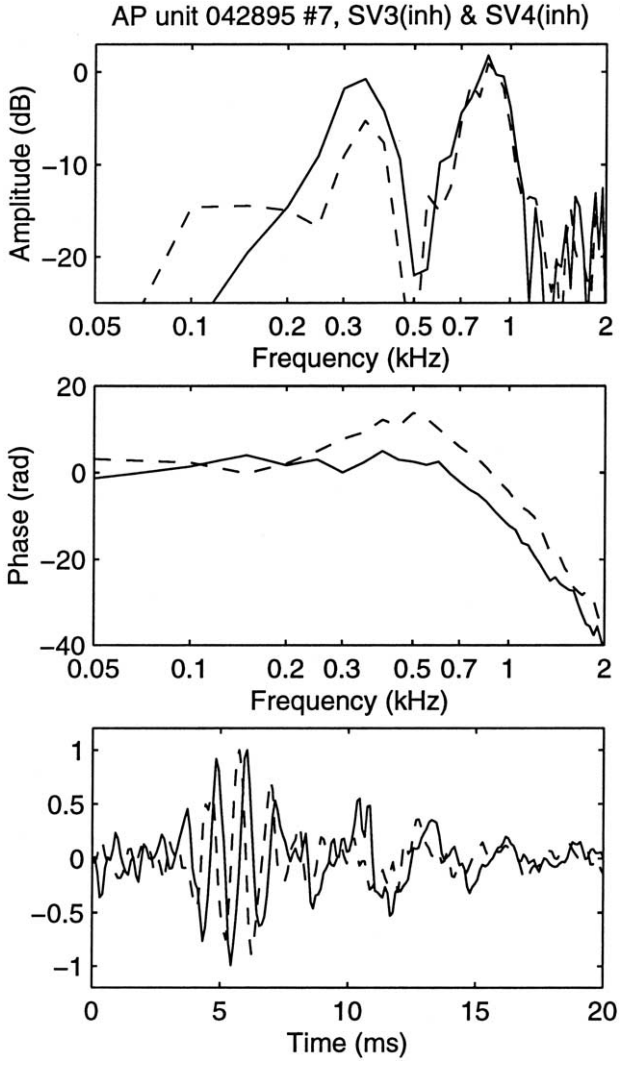

Fig. 9. Third-ranking (solid line) and fourth-ranking (dashed line) singular vectors of the second-order Wiener kernel of Fig. 5, normalized as in Fig. 7, along with their DFTs. These vectors embody timing and tuning of suppression (vicinity of 5 ms, 800 Hz) and adaptation (beyond approximately 7 ms, 300 Hz).

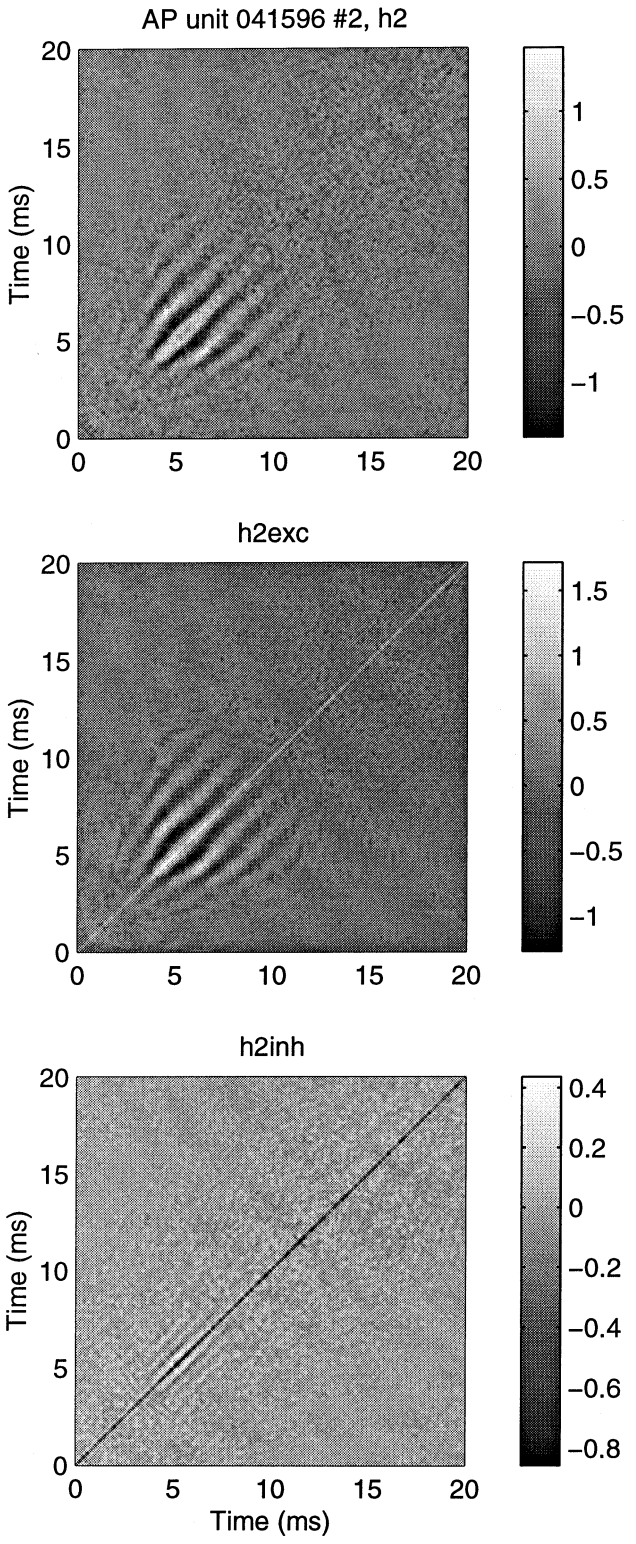

Fig. 10. Second-order Wiener kernel, along with its excitatory and inhibitory components, from another bullfrog amphibian-papillar unit.

component to the present instantaneous spike rate that is proportional to the square of the envelope of a linearly-filtered version of the stimulus constituents that occurred approximately 4–10 ms ago and had spectral energy in the vicinity of 560 Hz (see Fig. 12). The inhibitory component, h_{2inh}, shows a very faint pattern of adaptation (which was not represented cleanly by any singular vector) and a clear pattern of suppression. The latter is embodied in a subtractive component proportional to the square of the envelope of a linearly-filtered version of the stimulus constituent that occurred approximately 4–7 ms ago and had spectral energy in the vicinity of 1.2 kHz (see Fig. 13). The shape of the first-order kernel for this unit nearly matched that of SV_1 (Fig. 14, bottom panel), but the peak of the amplitude component of its DFT is shifted to approximately 500 Hz. We presume that SV_1 reflects the peripheral tuning up to the hair bundle, and that the high-frequency side of the corresponding amplitude DFT was shaved off by the low-pass filtering that occurs between the hair bundle and the afferent spike trigger. It is this low-pass filtering that evidently accounts for the reduction in phase-locking ability above approximately 500 Hz (Hillery and Narins, 1987; Weiss and Rose, 1988).

The second-order Wiener kernel described in Figs. 15 and 16 was taken over 23 500 spikes from a 160-Hz amphibian-papillar unit (in response to white noise, 70 dB SPL, 50 Hz to 1.8 kHz). As was observed consistently in low-frequency units, the shape of the highest-ranking singular vector, SV_1, matched very well that of the first-order Wiener kernel, h_1 (see Fig. 16). The

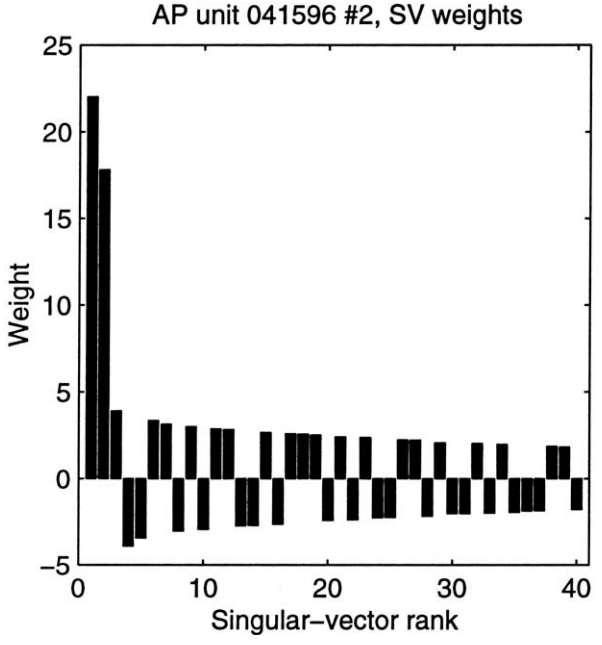

Fig. 11. Weights for the 40 highest-ranking singular vectors of the Wiener kernel of Fig. 10.

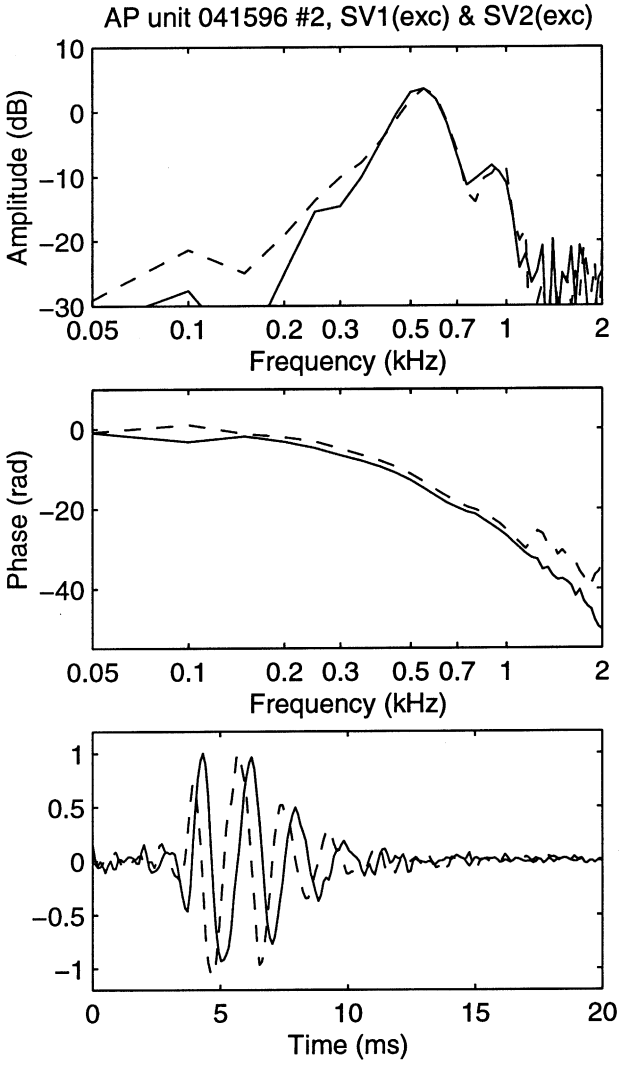

Fig. 12. Highest-ranking pair of singular vectors of the second-order Wiener kernel of Fig. 10, normalized as in Fig. 7, along with their DFTs. These two vectors form an excitatory quadrature pair, embodying excitatory timing and tuning.

excitatory component of h_2 reflects square-law distortion of the response phase-locked to the filtered stimulus waveform. Although the inhibitory component of h_2 clearly reflects both suppression and adaptation, neither was represented cleanly in any singular vector (see Appendix A.3).

5. Conclusions

In the now-classical studies that defined our current state of knowledge about the stimulus–response properties of auditory afferent axons, the three fundamental phenomena – excitation, adaptation and suppression were examined independently with simple stimuli. Although it was widely acknowledged that complex

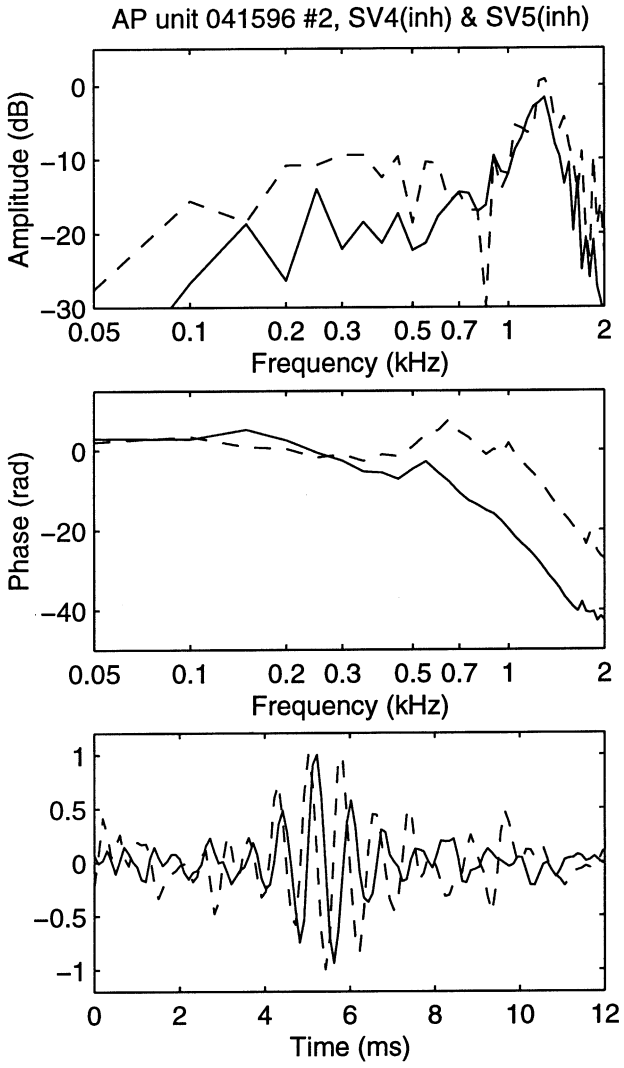

Fig. 13. Fourth-ranking (solid line) and fifth-ranking (dashed line) singular vectors of the second-order Wiener kernel of Fig. 10, both normalized as in Fig. 7, along with their DFTs. These vectors embody timing and tuning of suppression (vicinity of 5 ms, 1200 Hz).

stimuli would evoke all three phenomena at once, it was not clear that their effects in such a situation would be separable. The stimuli invoked in our studies were very complex (continuous, non-repeating, random acoustic waveforms with broad spectra). Our results show that excitation, adaptation and suppression indeed do occur together in response to these stimuli; and their effects appear simultaneously in the second-order Wiener kernel. We also have found that singular-value decomposition allows us to pull these effects apart easily and to study them individually – revealing not only their spectral relationships, but also their temporal relationships.

For each of the three amphibian-papillar units used as examples in this paper (Figs. 5, 10 and 14) the pattern of parallel diagonal lines representing suppression was shorter in duration than the pattern representing excitation, and it was simultaneous with the part of the excitatory pattern closest to the origin (closest to the time of the spike). This implies that the impact of a transient suppressive stimulus on the response to a transient excitatory stimulus is effective if the suppressive stimulus is applied toward the end of the excitatory stimulus. This relationship was observed consistently in the second-order Wiener kernels of bullfrog amphibian-papillar units. In the inhibitory component of the second-order kernel of Fig. 5, the transition from adaptation to suppression is accompanied by converging lines. This pattern was common among the second-order Wiener kernels for amphibian-papillar units. We were unable to create similar patterns in second-order kernels constructed from two quadrature pairs of filter functions tuned to different frequencies and partially

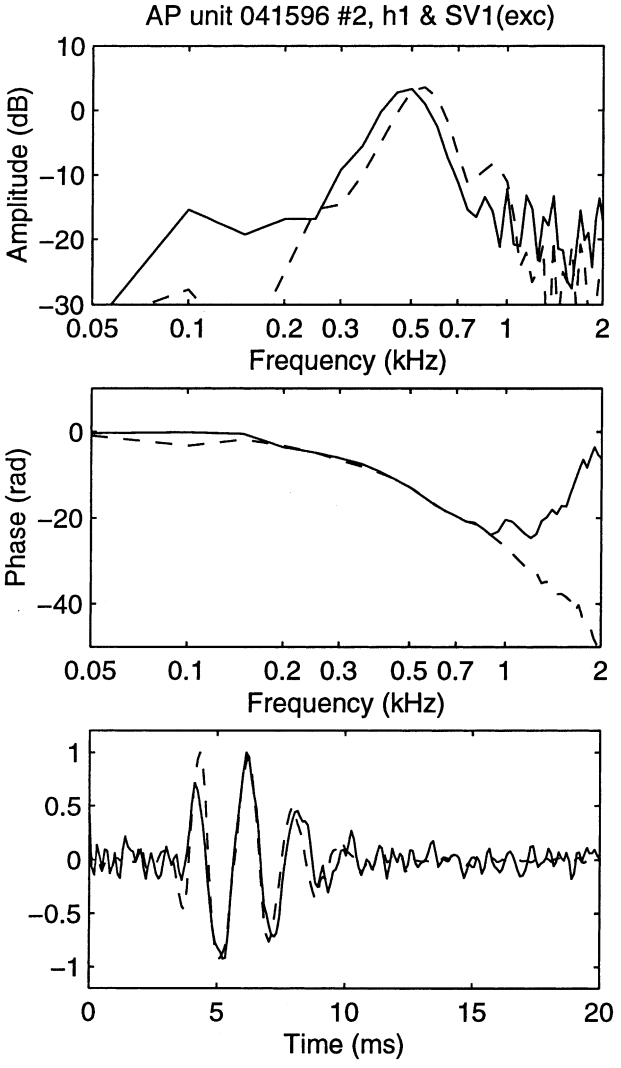

Fig. 14. First-order Wiener kernel (solid line) and highest-ranking singular vector of the second-order Wiener kernel of Fig. 10, both normalized as in Fig. 7, along with their DFTs.

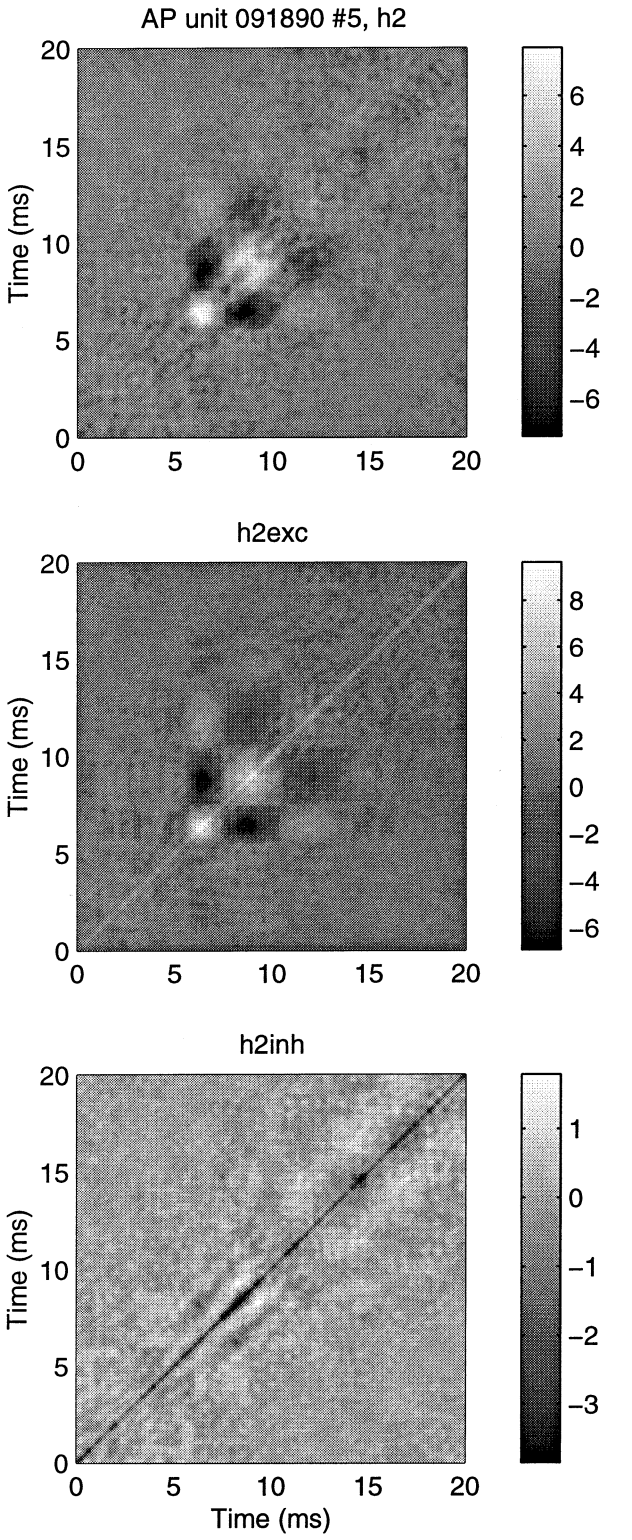

Fig. 15. Second-order Wiener kernel, along with its excitatory and inhibitory components, from a low-frequency amphibian-papillar unit.

overlapping in time. Therefore we tentatively take it to imply the presence of a rapid upward glide in the frequency of sensitivity during the transition from adaptation to suppression. It suggests the possibility that, in the bullfrog amphibian papilla, adaptation and suppression are linked. Sinusoidal steady-state analysis had suggested the same thing, along with the conclusion that both adaptation and suppression in the bullfrog amphibian papilla are reflected largely in negative dc shifts in the instantaneous spike rate (Lewis, 1986).

In our attempts to reconstruct the transition from adaptation to suppression in inhibitory kernels, we employed gammatone filter functions, which have no frequency glides of their own. A reviewer pointed out that downward frequency glides appear in all of the ob-

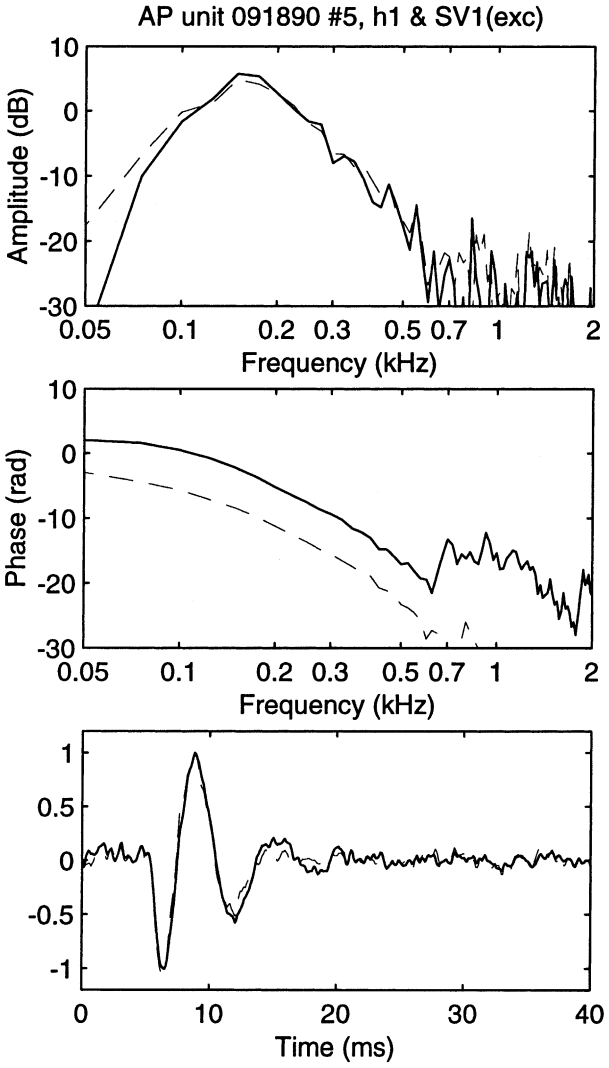

Fig. 16. First-order Wiener kernel (bottom panel, solid line) and the highest-ranking singular vector (bottom panel, dashed line) of the second-order Wiener kernel of the unit of Fig. 15. The corresponding DFTs are shown in the top and middle panels.

served excitatory filter functions that we present in this paper (see bottom panels of Figs. 7, 8, 12, 14 and 16). The reviewer suggested further that since the tuning for adaptation should be similar to that for excitation, the upward frequency glide in the inhibitory transition (which occurs in reverse time, i.e. from right to left in the inhibitory kernel) might simply mirror the downward frequency glide (which occurs in forward time) in the excitatory filter function. This is an interesting possibility. In the case of the unit of Fig. 5, however, the downward glide in excitatory filter function (seen in both the bottom panel of Fig. 7 and the center panel of Fig. 5) extends over a frequency change of approximately 20%. The frequency change in the apparent glide in the inhibitory transition (in the vicinity of 10 ms) in the bottom panel of Fig. 5 is more than 100%. Thus the glide in the excitatory filter function may not be sufficient to account entirely for the apparent glide in the inhibitory transition. The possible relationship needs to be explored further, however.

Conspicuous downward frequency glides in excitatory filter functions are common in units from the bullfrog amphibian papilla (Lewis et al., 1990). Carney et al. (1999) reported their presence in the mammalian cochlea as well. Showing that they occur in units from the three organs (basilar papilla of the red-eared turtle, saccule of the bullfrog, and bullfrog amphibian papilla) where electrical resonances were first reported, Lewis et al. (1990) argued that they reflect tuning structures of high dynamic order – as opposed to simple resonances. The selective advantages of such tuning, where frequency discrimination is achieved by means of tuning band edges made steep by high dynamic order, have been discussed extensively (e.g. see Lewis, 1990).

From the first- and second-order Wiener kernels, we found amphibian-papillar excitatory CFs ranging from approximately 100 Hz to approximately 1000 Hz. This is the same range found previously with tonal stimuli (Feng et al., 1975; Lewis et al., 1982). Studies of suppression with tonal stimuli in the frog amphibian papilla have largely focussed on reduction of the responses to tones at the excitatory CF when a second tone is presented simultaneously (two-tone suppression). Studies of the frequency dependence of the effectiveness of the suppressor tone led to the determination of suppressor CFs, which, in the bullfrog amphibian papilla, typically were 300 to 800 Hz higher than the excitatory CFs (Frishkopf and Goldstein, 1963; Feng et al., 1975; Capranica, 1976). That corresponds well to what we found in the second-order Wiener kernels from that organ.

Peristimulus–time histograms (PSTHs) commonly are used to display the time courses of adaptation for repeated, short-duration stimuli of constant amplitude. Although the general timing of adaptation implied by our results with second-order Wiener kernels is consistent with the general timing seen in such PSTHs for the bullfrog amphibian papilla (Megela and Capranica, 1981; Megela, 1984), the temporal details available in the PSTHs are not immediately apparent in the kernels or the singular vectors. To translate the kernels into PSTHs, one would substitute an expression for the repeated stimulus waveform, $p(t)$, into the Wiener series (Eq. 11). In general, one expects the Wiener series to provide good predictions of the PSTH as long as the root-mean-square amplitude of the stimulus waveform is comparable to that of the noise used to derive the kernels (for examples, see de Boer and de Jongh, 1978; Yamada et al., 1996; Yamada and Lewis, 1999). As it does in the mammalian cochlea (Lewis and Henry, 1995), however, adaptation in the bullfrog amphibian papilla involves both shifts in the dc spike-rate response and gain changes in the ac spike-rate response (Yu, 1991). Whereas the dc shifts are embodied in the inhibitory components of the second-order kernels, the ac gain changes are not. They are found in the dependence of K (in Eq. 3) on the level of the noise stimulus (Yamada, 1997).

Acknowledgements

The research reported here was supported by the National Institute of Deafness and Communicative Disorders (Grant DC-00112).

Appendix

A.1. Rephrasing singular-value decomposition for symmetric matrices

For singular-value decomposition we use the svd operation in MATLAB®, which in turn uses the LINPACK routine ZSVDC (Dongarra et al., 1979). For a square matrix, symmetric about the main diagonal, the operation decomposes the $n \times n$ matrix $\boldsymbol{X}$ into the following sum:

$$\boldsymbol{X} = \sum_{j=1}^{n} s_j \boldsymbol{u}_j \boldsymbol{v}_j^{\mathrm{T}} \tag{A1}$$

where both $\boldsymbol{u}_j$ and $\boldsymbol{v}_j$ are n-element column vectors; and s_j is a positive number, with $s_j \geq s_{j+1}$. Owing to the manner of construction of the singular-value decomposition and the symmetry of $\boldsymbol{X}$ about the main diagonal, either

$$\boldsymbol{u}_j = \boldsymbol{v}_j \tag{A2}$$

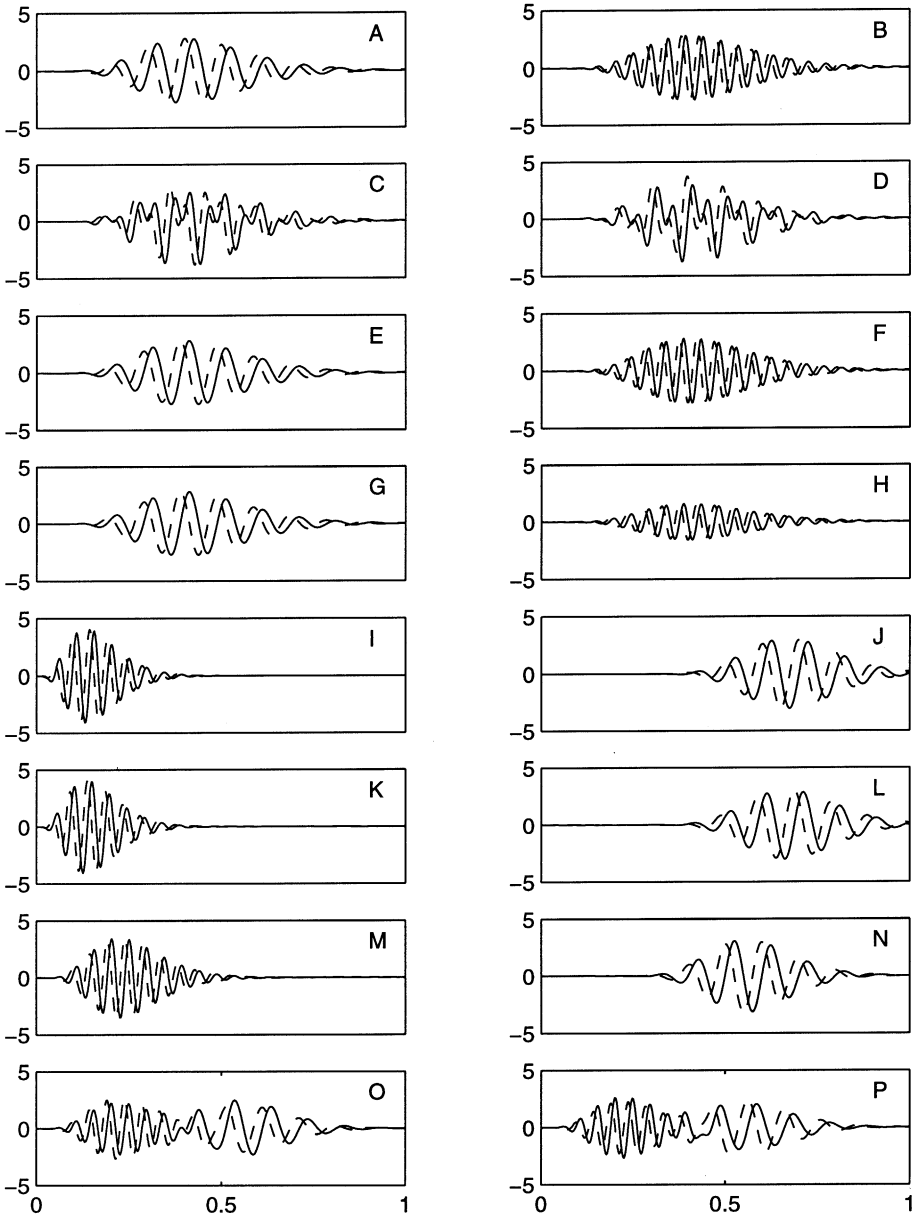

Fig. 17. Attempts to recover original filter functions by singular-value decomposition of simulated second-order Wiener kernels. A: Quadrature pair of gammatone functions with $\gamma_i = 8$, $\alpha_i = 20$, $f_i = 10$. B: Quadrature pair of gammatone functions with $\gamma_i = 8$, $\alpha_i = 20$, $f_i = 21$. The value of K in each case was set to make the root-mean-square (rms) value of the truncated function equal to 1.0. C–H: Singular vectors extracted from matrices constructed with various combinations of the waveforms in A and B (see text). I: Quadrature pair of gammatone functions with $\gamma_i = 4$, $\alpha_i = 30$, $f_i = 21$. J: Quadrature pair of gammatone functions with $\gamma_i = 30$, $\alpha_i = 45$, $f_i = 10$. Again, the value of K in each case was set to make the rms value of the truncated function equal to 1.0. K, L: Singular vectors extracted from the matrix constructed from the waveforms of I and J. M: Quadrature pair of gammatone functions with $\gamma_i = 6$, $\alpha_i = 27$, $f_i = 21$. N: Quadrature pair of gammatone functions with $\gamma_i = 28$, $\alpha_i = 45$, $f_i = 10$ – values of K set to make the rms values equal 1.0. O, P: Singular vectors extracted from the matrix constructed from the waveforms of M and N.

or

$$\boldsymbol{u}_j = -\boldsymbol{v}_j \tag{A3}$$

We have elected to rewrite the decomposition as follows:

$$\boldsymbol{X} = \sum_{j=1}^{n} \operatorname{sgn}[u_j(i)v_j(i)]s_j\boldsymbol{u}_j\boldsymbol{u}_j^{\mathrm{T}} = \sum_{j=1}^{n} k_j\boldsymbol{u}_j\boldsymbol{u}_j^{\mathrm{T}} \tag{A4}$$

with

$$k_j = \operatorname{sgn}[u_j(i)v_j(i)]s_j$$

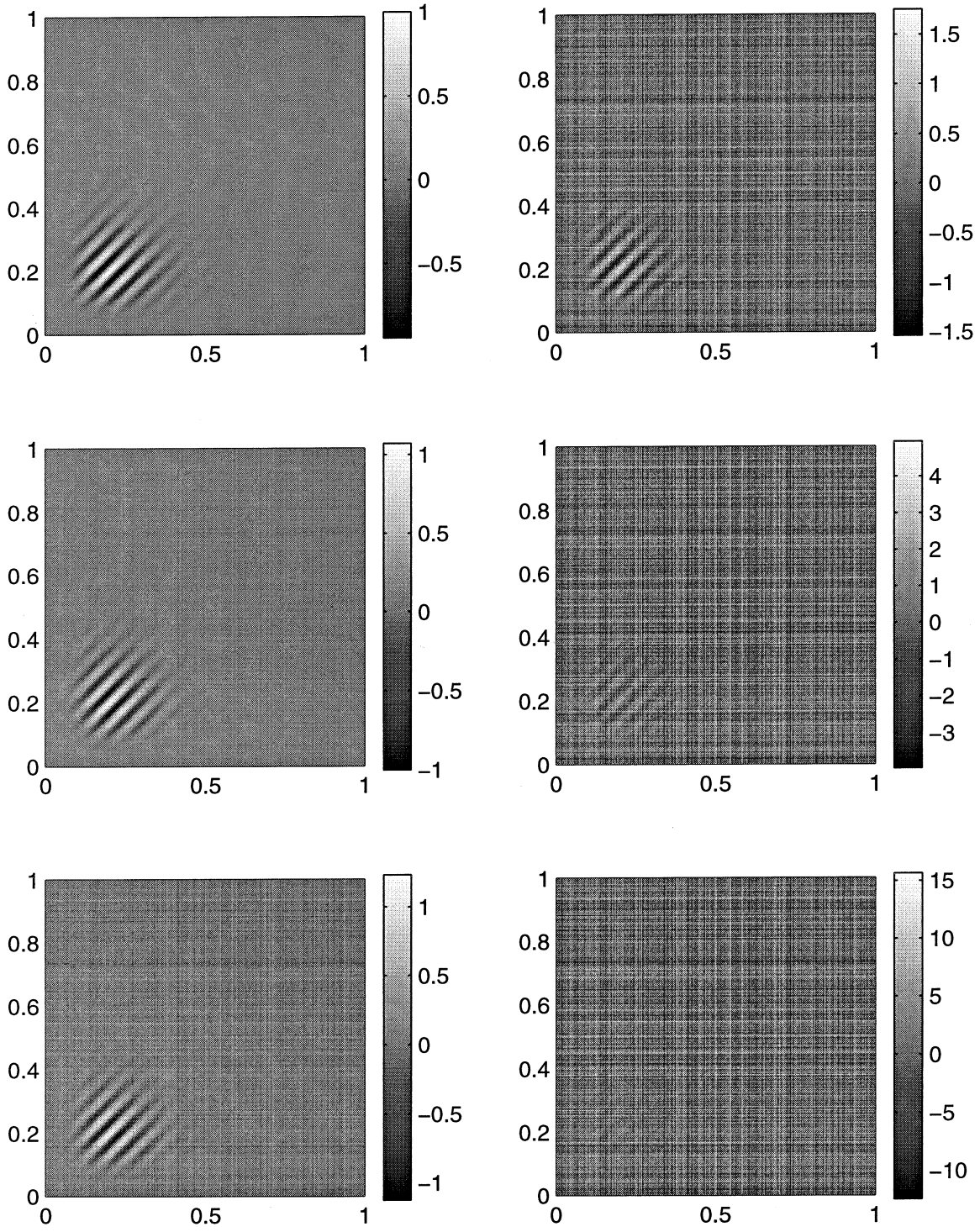

Fig. 18. Simulated second-order Wiener kernels with various amounts of additive noise (see text).

where $u_j(i)$ and $v_j(i)$ are the ith elements (non-zero elements) of column vectors $\boldsymbol{u}_j$ and $\boldsymbol{v}_j$, respectively, where i is any integer between 1 and n.

A.2. Extraction of individual filter functions from complex matrices

If one constructs an $n \times n$ matrix as the weighted sum of the outer products of a set of n-element vectors with themselves, then applies the MATLAB® svd operation

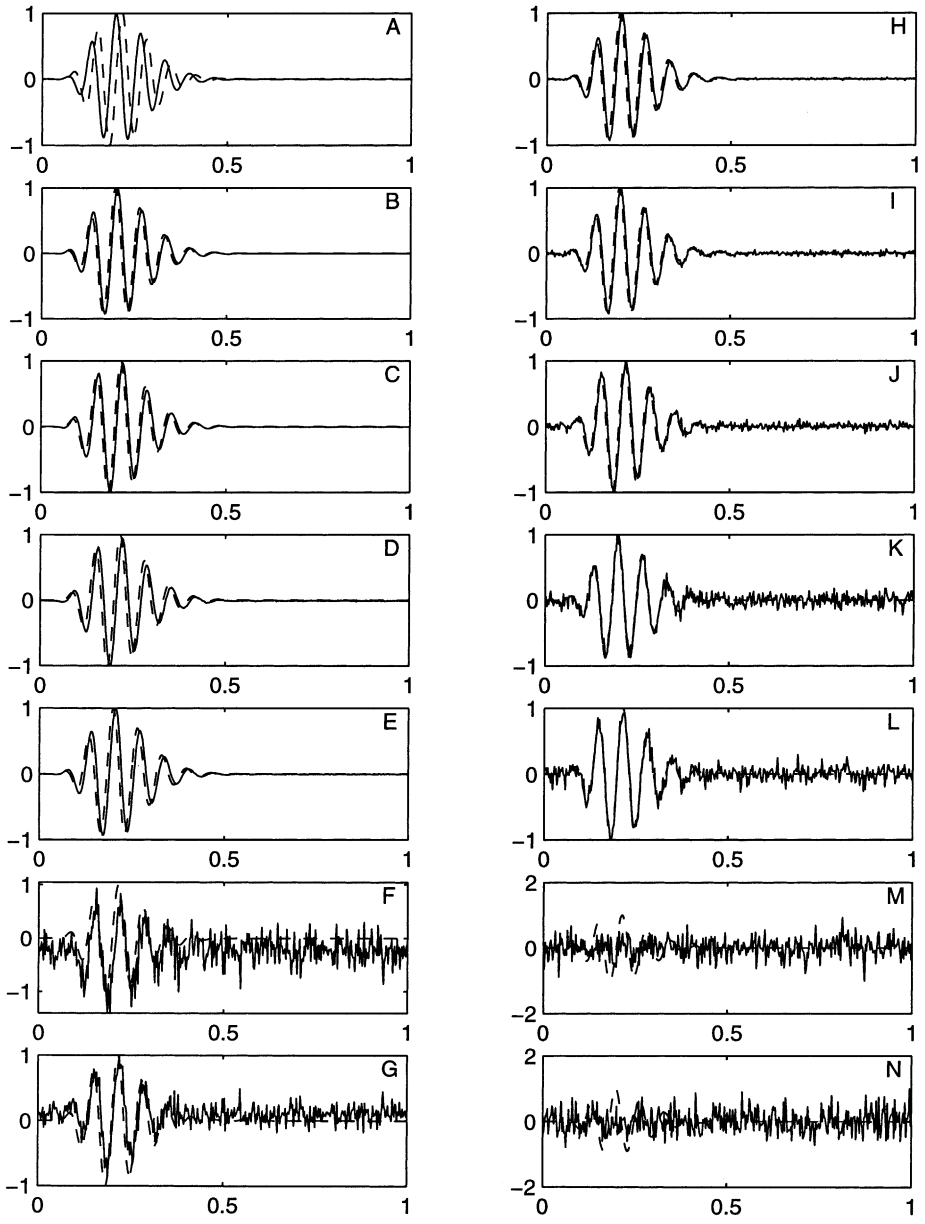

Fig. 19. Attempts to extract original filter functions by singular-value decomposition of the simulated second-order Wiener kernels in Fig. 18 (see text). A: Original filter functions (a quadrature pair). B–N: Extracted filter functions (solid lines), compared with originals (dashed lines).

to that matrix, the singular vectors, $\boldsymbol{u}_j$, that are computed will not necessarily be good matches to the vectors that went into the construction of the matrix. The singular-value decomposition operation is basically an optimization process, with the following steps (for symmetric matrices): (1) Find the n-element vector whose (positive or negative) outer product with itself gives the best fit to the $n\times n$ matrix (in the sense of having the least mean square error). (2) Subtract the (positive or negative) outer product of that vector with itself from the matrix. (3) Repeat steps 1 and 2 on the residual $n\times n$ matrix. (4) Continue this process until n such vectors have been found. There is no obvious reason to expect this process to systematically find individual filter functions embedded in backgrounds of other filter functions or noise. Nonetheless, experiments with second-order kernels simulated with gammatone functions show that singular-value decomposition is often able to do just that.

Fig. 17 shows examples based on quadrature pairs of truncated gammatone functions,

$$f_i(t) = \begin{cases} K_{i1} t^{\gamma_i} \mathrm{e}^{-\alpha_i t} \sin[2\pi f_i t] & 0<t\leq 1.0 \\ 0 & t\leq 0,\ t>1.0 \end{cases}$$

$$g_i(t) = \begin{cases} K_{i2} t^{\gamma_i} \mathrm{e}^{\alpha_i t} \cos[2\pi f_i t] & 0<t\leq 1.0 \\ 0 & t\leq 0,\ t>1.0 \end{cases} \qquad \text{(A5)}$$

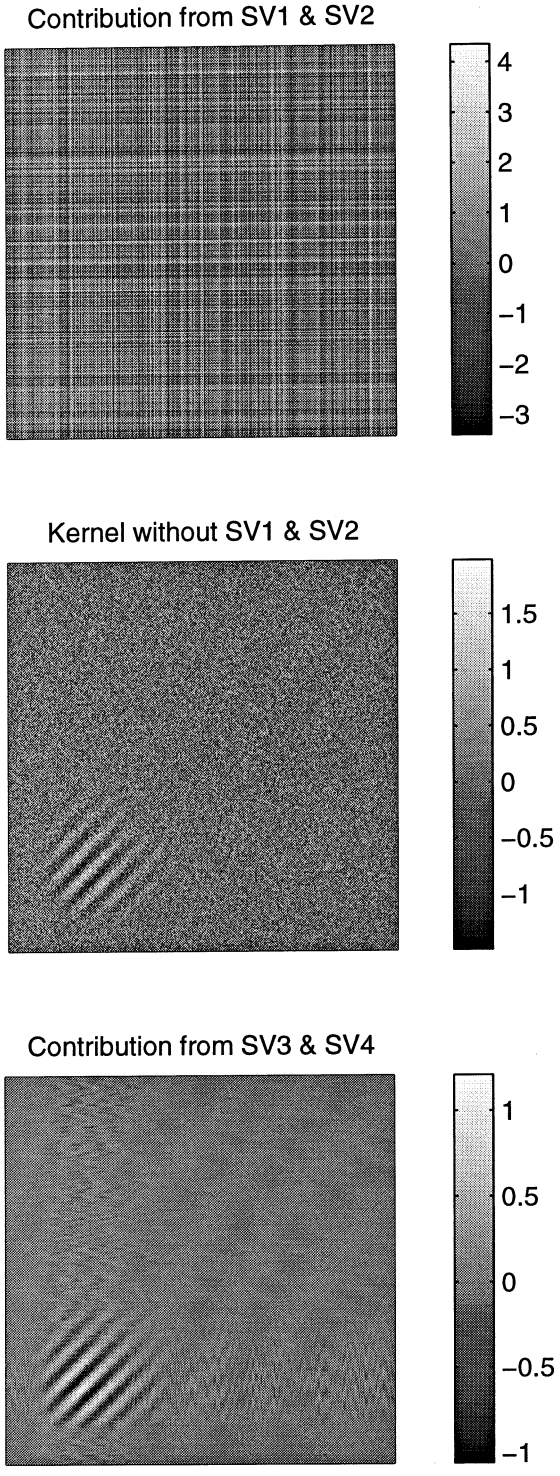

Fig. 20. Uncovering the filter functions in the very noisy second-order Wiener kernel of the center, right-hand panel of Fig. 18.

combined in various ways to simulate second-order kernels, which then were subjected to singular-value decomposition. Fig. 17C and D show the four non-zero singular vectors that emerged from singular-value decomposition of a matrix created as the sum of the outer products of each of the four truncated waveforms in Fig. 17A and B with itself. Notice that the original waveforms (Fig. 17A and B) did not emerge intact; each of the singular vectors (Fig. 17C and D) is a composite of the originals. This is a common observation when the two original pairs represent the same polarity of response (either both excitatory or both inhibitory), are of comparable amplitude, and have considerable temporal overlap, as these do. By contrast, when the two waveform pairs represent opposite effects (one being excitatory, the other inhibitory) or are sufficiently different in amplitude, then singular-value decomposition tends to extract them intact from the matrix. Fig. 17E and F, for example, show the four non-zero singular vectors that emerged from singular-value decomposition of a matrix created in the same way, but with the waveform pair in Fig. 17A being excitatory, that in Fig. 17B being inhibitory. Fig. 17G and H show the four non-zero singular vectors that emerged from singular-value decomposition of a matrix created in the same way, but with both waveform pairs being excitatory and the amplitude of the pair in Fig. 17B being reduced by 5 dB.

The original waveforms also tend to emerge intact if they have adequate temporal separation. For example, Fig. 17K and L show the four non-zero singular vectors that emerged from singular-value decomposition of a matrix created as the sum of the outer products of each of the four truncated waveforms in Fig. 17I and J with itself. By contrast, when the matrix was created in the same way from the truncated waveform pairs in Fig. 17M and N, which have somewhat greater temporal overlap, singular-value decomposition failed to extract them intact. What emerged instead were the four singular vectors in Fig. 17O and P, which are composites of those in Fig. 17M and N.

A.3. Extracting filter functions from noisy matrices

By virtue of the manner in which they are constructed, second-order Wiener kernels derived from noise stimuli are themselves noisy. The noise and filter functions are contemporaneous; and, occasionally, the pattern generated by the filter function may appear faintly in a noisy background. Even when the pattern is faint, singular-value decomposition often is successful in extracting the filter function relatively cleanly – typically as a singular vector with rank lower than two. In Figs. 18–20, we have simulated situations with purely additive noise. The 400×400 matrix in the upper left-hand panel of Fig. 18 was generated as the sum of the outer products of the two eighth-order gammatone filter functions in Fig. 19A. This matrix was then normalized to make the value of its largest element equal 1.0. In the subsequent panels, this matrix was added to a 400×400 noise matrix whose weight was varied in

10-dB steps. The noise matrix was created from a 400×400 array of random numbers, selected from a uniform distribution ranging from 0 to 1. The outer product of each column vector with itself was added to that of each of the 399 other column vectors. This was repeated for all 400 row vectors, and the result subtracted from the sum for column vectors.

Fig. 19B and C show the filter functions (solid lines) that were extracted by singular-value decomposition of the noiseless matrix in the upper left-hand panel of Fig. 18. The dashed line in each panel from Fig. 19B–N shows the corresponding original waveform (from Fig. 19A). Fig. 19D and E show the filter functions (solid lines) extracted from the matrix on the center left panel of Fig. 18; in this case the rms value of the added noise was −30 dB re 1.0. Fig. 19F, G and H show the filter functions extracted from the bottom left-hand panel of Fig. 18; in this case the rms value of the added noise was −20 dB re 1.0. Notice that one member of the filter–function pair was extracted cleanly (Fig. 19H), but the other member was extracted in two installments, each mixed with substantial noise. In Fig. 19I–L, with the noise level increased further (−10 dB for Fig. 19I, J; 0 dB for Fig. 19K, L), the filter functions once again were extracted cleanly. The corresponding matrices are shown in the upper (−10 dB) and center (0 dB) right-hand panels of Fig. 18. In the lower right-hand panel of Fig. 18 the rms value of the noise was 10 dB re 1.0. In this case, the filter functions were not obviously represented in any of the singular vectors (e.g. Fig. 19M, N).

In Fig. 19B, C and D, E, the filter functions were extracted as the highest-ranking pair of singular vectors (SV_1 and SV_2). In Fig. 19I, J and K, L, they were extracted as SV_3 and SV_4 (SV_1 and SV_2 in both cases reflected pure noise). The situation in Fig. 19F–H was transitional: Fig. 19F (SV_1), Fig. 19G (SV_4), Fig. 19H (SV_3). Fig. 20 shows the manner in which pure noise was peeled away (by singular-value decomposition) from the matrix in the center right-hand panel of Fig. 17. The center panel of Fig. 20 shows that matrix after removal of the contributions from SV_1 and SV_2.

References

Capranica, R.R., 1976. Morphology and physiology of the auditory system. In: Llinas, R., Precht, W. (Eds.), Frog Neurobiology. Springer, Berlin, pp. 551–575.

Carney, L.H., McDuffy, M.J., Shekhter, I., 1999. Frequency glides in the impulse responses of auditory-nerve fibers. J. Acoust. Soc. Am. 105, 2384–2391.

de Boer, E., de Jongh, H.R., 1978. On cochlear encoding: potentialities and limitations of the reverse-correlation technique. J. Acoust. Soc. Am. 63, 115–135.

de Boer, E., Kuyper, P., 1968. Triggered correlation. IEEE Trans. BME 15, 169–179.

Dongarra, J.J., Bunch, J.R., Moler, C.B., Stewart, G.W., 1979. LINPACK User's Guide. SIAM, Philadelphia, PA.

Eggermont, J.J., 1993. Wiener and Volterra analyses applied to the auditory system. Hear. Res. 66, 177–201.

Feng, A.S., Narins, P.M., Capranica, R.R., 1975. Three populations of primary auditory fibers in the bullfrog (*Rana catesbeiana*): their peripheral origins and frequency sensitivities. J. Comp. Physiol. 100, 221–229.

Frishkopf, L.S., Goldstein, M.H., Jr., 1963. Responses to acoustic stimuli from single units in the eighth nerve of the bullfrog. J. Acoust. Soc. Am. 35, 1219–1228.

Hillery, C.M., Narins, P.M., 1987. Frequency and time domain comparison of low-frequency auditory fiber responses in two anuran amphibians. Hear. Res. 35, 233–248.

Lewis, E.R., 1986. Adaptation, suppression and tuning in amphibian acoustical fibers. In: Moore, B.C.J., Patterson, R.D. (Eds.), Auditory Frequency Selectivity. Plenum, New York, pp. 129–136.

Lewis, E.R., 1990. Electrical tuning in the ear. Comm. Theoret. Biol. 1, 253–273.

Lewis, E.R., Henry, K.R., 1995. Nonlinear effects of noise on phase-locked cochlear nerve responses to sinusoidal stimuli. Hear. Res. 92, 1–16.

Lewis, E.R., Leverenz, E.L., Koyama, H., 1982. The tonotopic organization of the bullfrog amphibian papilla, an auditory organ lacking a basilar membrane. J. Comp. Physiol. 145, 437–445.

Lewis, E.R., Sneary, M.G., Yu, X.Y., 1990. Further evidence for tuning mechanisms of high dynamic order in lower vertebrates. In: Dallos, P., Geisler, C.D., Matthews, J.W., Ruggero, M.A., Steele, C.R. (Eds.), The Mechanics and Biophysics of Hearing. Springer, Berlin, pp. 139–146.

Marmarelis, P.Z., Marmarelis, V.Z., 1978. Analysis of Physiological Systems: The White-Noise Approach. Plenum, New York.

Megela, A.L., 1984. Diversity of adaptation patterns in responses of eighth nerve fibers in the bullfrog, *Rana catesbeiana*. J. Acoust. Soc. Am. 75, 1155–1162.

Megela, A.L., Capranica, R.R., 1981. Response patterns to tone bursts in peripheral auditory systems of anurans. J. Neurophysiol. 46, 465–478.

Rugh, W., 1981. Nonlinear System Theory: The Volterra/Wiener Approach. Johns-Hopkins Press, Baltimore, MD.

Schetzen, M., 1980. The Volterra and Wiener Theories of Nonlinear Systems. John Wiley and Sons, New York.

van Dijk, P., Wit, H.P., Segenhout, J.M., 1997a. Dissecting the frog inner ear with Gaussian noise. I. Application of high-order Wiener-kernel analysis. Hear. Res. 114, 229–242.

van Dijk, P., Wit, H.P., Segenhout, J.M., 1997b. Dissecting the frog inner ear with Gaussian noise. II. Temperature-dependence of inner-ear function. Hear. Res. 114, 243–251.

van Dijk, P., Wit, H.P., Segenhout, J.M., Tubis, A., 1994. Wiener kernel analysis of inner-ear function in the American bullfrog. J. Acoust. Soc. Am. 95, 904–919.

Weiss, T.F., Rose, C., 1988. A comparison of synchronization filters in different auditory receptor organs. Hear. Res. 33, 175–180.

Yamada, W.M., 1997. Second-order Wiener Kernel Analysis of Auditory Afferent Axons of the North American Bullfrog and Mongolian Gerbil Responding to Noise. Doctoral dissertation, Graduate Group in Neurobiology, University of California, Berkeley, CA.

Yamada, W.M., Lewis, E.R., 1999. Predicting the temporal responses of non-phase-locking bullfrog auditory units to complex acoustic waveforms. Hear. Res. 130, 155–170.

Yamada, W.M., Wolodkin, G., Lewis, E.R., Henry, K.R., 1996. Wiener-kernel analysis and the singular-value decomposition. In: Lewis, E.R., Long, G.R., Lyon, R.F., Narins, P.M., Steele, C.R., Hecht-Poinar, E. (Eds.), Diversity in Auditory Mechanics. World Scientific Press, Singapore, pp. 111–118.

Yu, X.Y., 1991. Signal Processing Mechanics in Bullfrog Inner Ear Inferred from Neural Spike Trains. Doctoral dissertation, Department of Electrical Engineering and Computer Science, University of California, Berkeley, CA.